

An NIR Fluorescence Turn-on and MRI Bimodal Probe for Concurrent Real-time in vivo Sensing and Labeling of β -Galactosidase

Qiao Yu⁺, Lei Zhang⁺, Mou Jiang, Long Xiao, Yunhui Xiang, Ruifang Wang, Zhaoqing Liu, Rui Zhou, Minghui Yang, Conggang Li, Maili Liu, Xin Zhou, and Shizhen Chen*

Abstract: To realize sensing and labeling biomarkers is quite challenging in terms of designing multimodal imaging probes. In this study, we developed a novel β -galactosidase (β -gal) activated bimodal imaging probe that combines near-infrared (NIR) fluorescence and magnetic resonance imaging (MRI) to enable real-time visualization of activity in living organisms. Upon β -gal activation, Gal-Cy-Gd-1 exhibits a remarkable 42-fold increase in NIR fluorescence intensity at 717 nm, allowing covalent labeling of adjacent target enzymes or proteins and avoiding molecular escape to promote probe accumulation at the tumor site. This fluorescence reaction enhances the longitudinal relaxivity by approximately 1.9 times, facilitating high-resolution MRI. The unique features of Gal-Cy-Gd-1 enable real-time and precise visualization of β -gal activity in live tumor cells and mice. The probe's utilization aids in identifying in situ ovarian tumors, offering valuable assistance in the precise removal of tumor tissue during surgical procedures in mice. The fusion of NIR fluorescence and MRI activation through self-immobilizing target enzymes or proteins provides a robust approach for visualizing β -gal activity. Moreover, this approach sets the groundwork for developing other activatable bimodal probes, allowing real-time in vivo imaging of enzyme activity and localization.

Introduction

Ovarian cancer ranks as the fifth most prevalent cause of cancer-related mortality and stands among the top three gynecological malignancies, exhibiting high fatality rates.^[1] Timely and accurate diagnosis of ovarian cancer at an early stage poses a significant challenge, as it plays a crucial role in effective treatment.^[2] Early-stage cancer often correlates with altered levels of specific biomarkers such as enzymes, pH, metal ions, oxygen, glutathione (GSH), etc.^[3] Detecting these tumor-associated biomarkers is vital for precise cancer diagnosis and treatment.^[4] Among these biomarkers, enzymes are fundamental players in biological systems and serve as major indicators of various diseases.^[5] For example, β -galactosidase (β -gal), an essential glycoside hydrolase

encoded by the lacZ gene and localized in lysosomes, holds significance as a biomarker, being overexpressed in primary ovarian cancer cells and senescent cells.^[6] In this regard, the development of probes for β -gal detection and imaging is paramount for early detection of ovarian cancer.^[7] However, despite early advances in the development of molecular probes for its detection, these structures mainly utilize only single-modality imaging techniques, which suffer from limitations in simultaneously addressing sensitivity, resolution, and penetration depth, making precise measurements of molecules in living organisms challenging.^[8]

The concept of multimodal molecular imaging integrates the preponderance of different imaging modalities to overcome the limitations of single-modal approaches.^[9] For instance, near-infrared (NIR) fluorescence imaging provides highly sensitive imaging for detecting low concentrations of tumor-associated biomarkers like overexpressed enzymes, aiding in image-guided tumor surgeries.^[10] On the other hand, magnetic resonance imaging (MRI) produces anatomical images with excellent tissue penetration depth and high spatial resolution, facilitating the preoperative detection of deep-seated tumors.^[11] Combining these two imaging modalities enables highly sensitive imaging of deep tumors.^[12] However, current activatable imaging probes tend to diffuse or translocate out of the cell from the initial active site of the enzyme after the enzyme response.^[13] This phenomenon reduces the signal-to-background ratio (SBR) for in vivo enzyme activity imaging. For the past twenty years, many activated probes have been developed either by fluorescence or MRI.^[14] Moreover, designing small molecule probes that can activate NIR fluorescence and MRI signals upon

[*] Q. Yu,⁺ L. Zhang,⁺ M. Jiang, L. Xiao, Y. Xiang, R. Wang, Z. Liu, R. Zhou, M. Yang, C. Li, M. Liu, X. Zhou, S. Chen
Key Laboratory of Magnetic Resonance in Biological Systems, State Key Laboratory of Magnetic Resonance and Atomic and Molecular Physics, National Center for Magnetic Resonance in Wuhan, Wuhan Institute of Physics and Mathematics, Innovation Academy for Precision Measurement Science and Technology, Chinese Academy of Sciences-Wuhan National Laboratory for Optoelectronics, Huazhong University of Science and Technology, Wuhan 430071 (P. R. China)
E-mail: chenshizhen@wipm.ac.cn

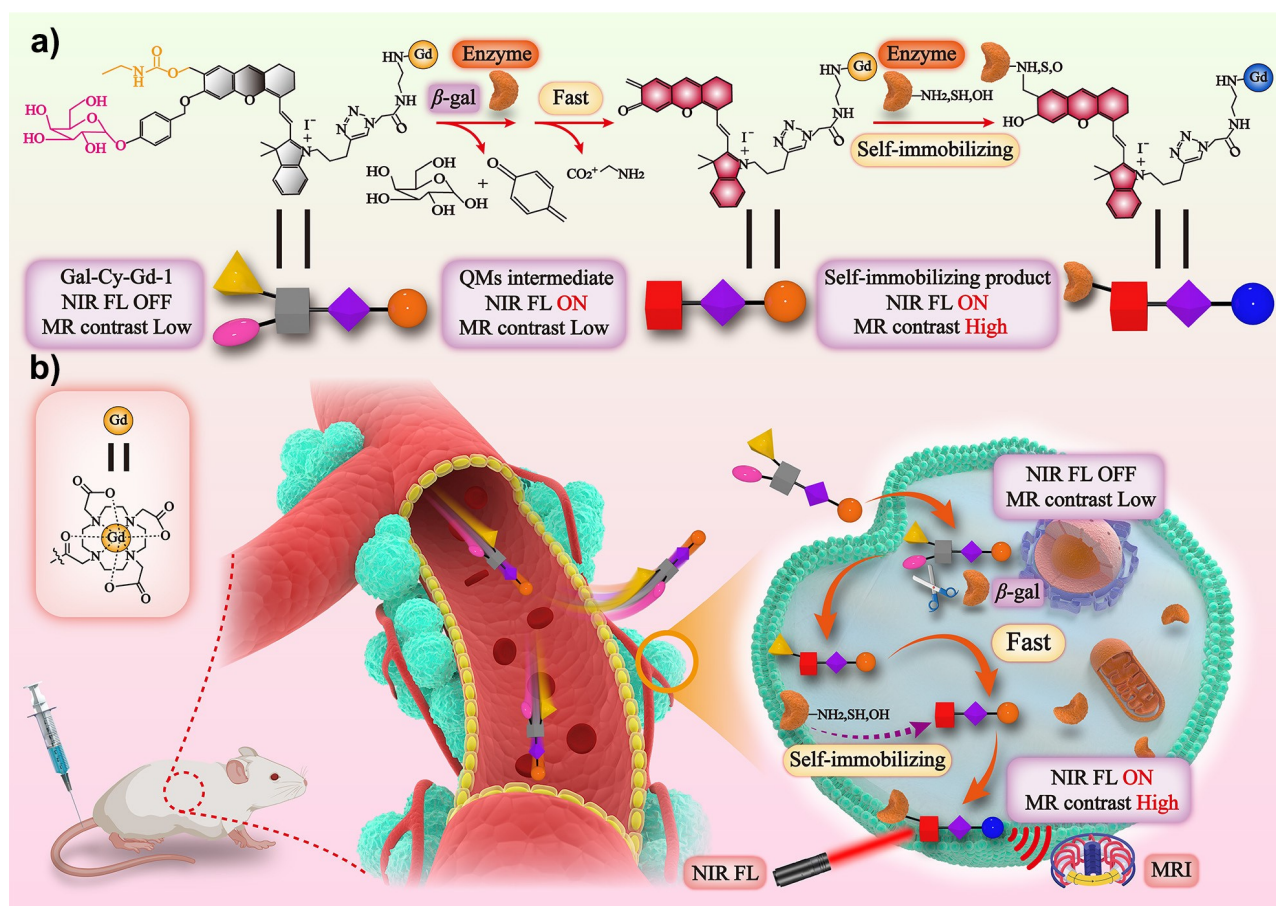
L. Zhang,⁺ L. Xiao, Y. Xiang, R. Wang, Z. Liu, R. Zhou, M. Yang, C. Li, M. Liu, X. Zhou, S. Chen
University of Chinese Academy of Sciences, Beijing 100049 (P. R. China)

[†] These authors contributed equally to this work.

interaction with tumor cells remains challenging since the signal-activated mechanism is different between fluorescent and relaxation-based MR contrast agents. In order to tackle the problem, a new strategy is urgently needed to design activatable small molecule fluorescence/MRI dual-modality imaging probes that exhibit high tumor permeability and accumulation. In recent years, a large amount of research has been reported on molecular imaging probes constructed using the strategy of stimulus-triggered in situ self-assembly of small molecules to form nanostructures, in which the longitudinal relaxivity could be increased as the rotational time decreased.^[15] Quinone methides (QMs) are transient molecules with very high electrophilicity. By utilizing an activatable NIR fluorophore as a precursor to QMs, these fluorescent probes substantially enhance fluorescence intensity and covalently label nearby target enzymes or proteins upon selective activation of the enzyme.^[16] This limits the rapid diffusion of the activated probes from the site of interest in a highly dynamic in vivo system, allowing visualization of enzyme activity in a dynamic environment. From

the point of T_1 -based MR contrast agent designing view, the restricted rotation of the molecule and prolonged rotational correlation time after anchoring the small molecule contrast agent to the target enzyme or protein lead to enhanced MR signals.

In light of this feature, in this work, we present the design, synthesis, and assessment of Gal-Cy-Gd-1, a bimodal probe integrating fluorescence and MR, capable of sensing and labeling β -gal. The probe was crafted by employing click chemistry to conjugate the urethane leaving group containing Hemi-Cy to Gd-DOTA. Gal-Cy-Gd-1 exhibited remarkable sensitivity and selectivity towards β -gal, forming an intermediate structure of QMs upon interaction. This intermediate displayed heightened reactivity, rendering it susceptible to nucleophilic group attacks at external protein residues. Consequently, the compounds were anchored to proteins, accompanied by a turn-on fluorescence signal and enhanced longitudinal relaxivity. In vivo evaluation of Gal-Cy-Gd-1 for bimodal β -gal imaging was conducted on ovarian cancer model mice, demonstrating promising results.



Scheme 1. Schematic illustration of a β -gal-activatable bimodal NIR fluorescence (FL)/MR probe for in vivo imaging. (a) Chemical structure of Gal-Cy-Gd-1 and proposed β -gal-mediated fluorogenic reaction and self-immobilization of protein-anchored Gal-Cy-Gd-1 showing enhanced NIR FL and MRI contrast. (b) Proposed mechanism of Gal-Cy-Gd-1 for NIR FL/MR bimodality imaging of β -gal-positive tumor cells in vivo. After systemic administration in mice, Gal-Cy-Gd-1, as a small molecule, can easily cross blood vessels and diffuse into tumor tissue. In tumor cells expressing high levels of β -gal, Gal-Cy-Gd-1 was hydrolyzed from the glycosidic bond by intracellular β -gal and rapidly formed QMs intermediates, which were subsequently attacked by nucleophilic groups on the enzyme, anchoring onto the enzyme and prolonging retention of the compound in tumor tissue, resulting in high signal intensity of NIR-FL and MRI contrast.

Moreover, the probe facilitated NIR fluorescence-guided real-time surgical resection of in situ ovarian cancer. This innovative approach plays a crucial role in designing bioresponsive probes capable of both sensing and labeling with imaging capabilities.

Results and Discussion

The β -gal responsive self-immobilized bimodal probe, Gal-Cy-Gd-1, comprises the following components: (1) a β -gal recognition site and self-immobilized linker, (2) a NIR fluorophore before quenching, (3) an ethyl carbamate leaving group, and (4) a paramagnetic DOTA-Gd chelate for MRI applications (Scheme 1). This tandem sensing and labeling strategy enables the probe to respond in the presence of β -gal. The corresponding control molecule Gal-Cy-Gd-2 consisted of a Hemi-Cy fluorophore and a Gd-

DOTA complex but without the urethane leaving group, preventing quinones' formation (Figure S1). And the final probes were characterized by liquid chromatography and mass spectrometry (LC-MS) (Figure S2).

Gal-Cy-Gd-1 alone is highly soluble in both water and aqueous buffer solution. The probe itself displays two absorption peaks at 607 nm and 656 nm, with weak NIR fluorescence attributed to the presence of β -galactose closure groups, which hinder charge transfer within the Cy fluorophore. As expected, upon activation by β -gal, the probe exhibits a time-dependent shift in the UV/Vis absorption spectra, reaching 687 nm, and a significant fluorescence enhancement confirmed by LC analysis of the fluorescent product. The UV/Vis absorption and NIR fluorescence both reach their peaks after 80 minutes of incubation with β -gal (Figure 1a, b). The sensitivity of Gal-Cy-Gd-1 to β -gal in solution was then examined, revealing a gradual increase in fluorescence with rising β -

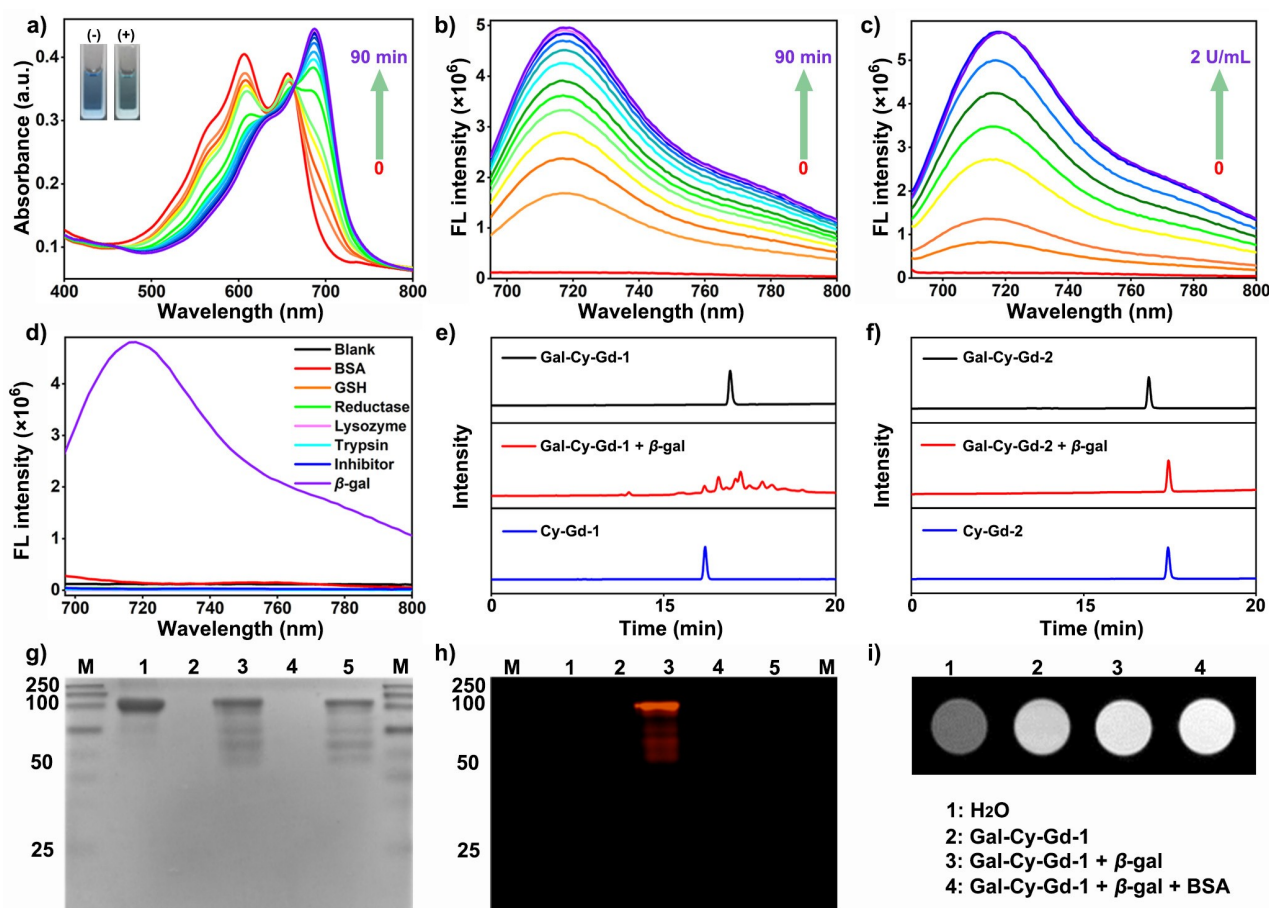


Figure 1. Characterization of Gal-Cy-Gd-1 in vitro. (a) UV-vis absorption and (b) fluorescence spectra of Gal-Cy-Gd-1 (5 μ M) incubated with β -gal (2 U/mL, 37 $^{\circ}$ C) for 0–90 min. $\lambda_{\text{ex}} = 685$ nm. (c) Fluorescence spectra of Gal-Cy-Gd-1 (5 μ M) following incubation with varying concentrations (0, 0.05, 0.1, 0.2, 0.4, 0.6, 0.8, 1.0 and 2.0 U/mL, 37 $^{\circ}$ C) of β -gal for 90 min. (d) Fluorescence spectra of Gal-Cy-Gd-1 (5 μ M) incubated with BSA, GSH, reductase, trypsin, lysozyme or β -gal together with its inhibitor D-(+)-ribonucleic acid-lactone in PBS (pH 7.4). HPLC traces of (e) Gal-Cy-Gd-1 (100 μ M) or (f) Gal-Cy-Gd-2 before and after incubation with β -gal (40 U/mL) at 37 $^{\circ}$ C for 90 min. (g) Coomassie blue staining and (h) fluorescence imaging of SDS-PAGE gel. The indicated enzyme was incubated with or without probes in PBS at 37 $^{\circ}$ C for 90 min. M: protein marker; 1: β -gal; 2: Gal-Cy-Gd-1; 3: Gal-Cy-Gd-1 + β -gal; 4: Gal-Cy-Gd-2; 5: Gal-Cy-Gd-2 + β -gal; $\lambda_{\text{ex}} = 680$ nm. (i) T_1 -weighted MR images of 1: H₂O, 2: Gal-Cy-Gd-1; 3: Gal-Cy-Gd-1 + β -gal and 4: Gal-Cy-Gd-1 + β -gal + BSA in PBS (pH 7.4).

gal concentration (Figure 1c). The fluorescence intensity at 717 nm shows a good linear correlation with β -gal concentration within the range of 0.1–1.0 U/mL, indicating that the enzyme concentration in this range could be quantified by fluorescence with a detection limit of 0.068 U/mL (Figure S3). Further investigations into the selectivity of Gal-Cy-Gd-1 for β -gal were carried out, demonstrating that, when compared to other representative enzymes (e.g., trypsin, bovine serum albumin (BSA), lysozyme, nitroreductase) and compounds (GSH and the β -gal inhibitor, D-(+)-ribonucleic acid-lactone), only β -gal expressively enhances the NIR fluorescence in PBS buffer (pH 7.4). Additionally, when D-(+)-ribonucleic acid-lactone (100 mM) inhibits β -gal activity, both fluorescence and MRI signals are significantly suppressed (Figure 1d, S4). Thus, Gal-Cy-Gd-1 exhibits specificity for β -gal in PBS buffer (pH 7.4). The stability of Gal-Cy-Gd-1 was also evaluated, and the results indicate no significant changes in LC peak area, fluorescence emission spectra, and T_1 values in DMEM medium containing 10% fetal bovine serum and various pH buffers, confirming its high stability (Figure S5, S6).

From docking calculations, the binding affinities of Gal-Cy-Gd-1 and Gal-Cy-Gd-2 are 11.3 and 9.8 kcal/mol respectively, indicating the higher binding activity for Gal-Cy-Gd-1, which is difficult to dissociate from the enzyme. Their corresponding docking modes are shown in Figure 2a, b with the probes in the binding pocket

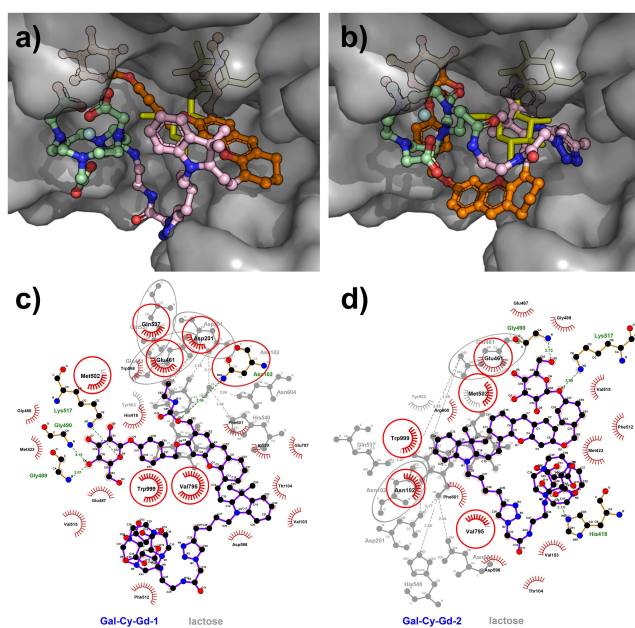


Figure 2. Docking modes of (a) Gal-Cy-Gd-1 and (b) Gal-Cy-Gd-2 to the β -gal with the lactose in the binding pocket from the X-ray structure (PDB ID: 1JYN). The β -gal and the lactose are shown in gray surface and yellow sticks. The probes are shown in sticks and balls model with N in blue, O in red and C in orange (head part), pink (middle part), light-green (tail part) respectively. LigPlot+ diagrams of (c) Gal-Cy-Gd-1 and (d) Gal-Cy-Gd-2 for the docking modes (colored) with superposition onto the lactose diagram (in gray).

complying with the lactose position from the experimental structure. In order to analyze the key residues that interacted with probes, we generated the diagrams on LigPlot+ for the docking modes with superposition onto the lactose diagram from the experimental structure (Figure 2c, d). Several key residues in the binding pocket are detected including Gln461, Met502, Trp999, Asn102 and Val795 which are identical to the lactose marked by red cycles. Additionally, the key residues Gln537 and Asp201 are only detected for Gal-Cy-Gd-1, which implies the discrepancy of the binding affinities by different probes. The previous studies discussed that the key residues such as the Asn102, Asp201, Trp999, Met502, and loop 794–804 are contributed to the substrate initially binding and penetrating deeply into the active binding pocket. Yet the Glu461 and Glu537 are suggested to act as key residues in catalysis. The docking results and identified key residues indicate that both Gal-Cy-Gd-1 and Gal-Cy-Gd-2 are capable of binding the β -gal. While, the additional interactions for the Gal-Cy-Gd-1 suggest that the Gal-Cy-Gd-1 is a good substrate to load tightly in the binding pocket and occupies a proper location to facilitate the catalysis processes.

To confirm the formation of QMs intermediates that label to surrounding proteins upon β -gal enzyme response, a control probe Gal-Cy-Gd-2 lacking a carbamate structure was synthesized. This pair of probes examined absorption and fluorescence emission spectra before and after incubation with β -gal. Gal-Cy-Gd-2 displayed similar absorption and fluorescence emission spectra before and after enzyme activation (Figure S7). β -mercaptoethanol (β -ME) was employed as an additional nucleophilic reagent to simulate the cellular environment containing nucleophilic proteins. As expected, the addition of β -ME induced an absorption peak shift and further enhanced the fluorescence of Gal-Cy-Gd-1 incubated with β -gal (Figure S7). High-performance liquid chromatography (HPLC) analysis of the samples before and after β -gal treatment revealed that Gal-Cy-Gd-1 produced a mixture of compounds containing the fluorophore Cy-Gd-1 (Figure 1e). In contrast, Gal-Cy-Gd-2 alone had only the free fluorophore Cy-Gd-2 (Figure 1f, S8 and S9). In-SDS gel fluorescence imaging of the incubated molecules with β -gal confirmed that co-incubation of Gal-Cy-Gd-1 with β -gal resulted in a robust NIR fluorescence signal, whereas β -gal alone, Gal-Cy-Gd-1 alone, and Gal-Cy-Gd-2 co-incubated with β -gal, as well as Gal-Cy-Gd-2 bands alone, showed no fluorescence (Figure 1g, h). These results demonstrated that Gal-Cy-Gd-1 has the capability to covalently attach to target enzymes or nearby proteins upon selective enzyme activation. Notably, this ability allowed for the retention of more activated fluorophores around the activation site without being limited by the number of nucleophilic residues of the target enzyme, facilitating in vivo imaging. As is known, a key parameter to increase the longitudinal relaxivity of a typical gadolinium-based contrast agent is to decrease the retention time (τ_R). In our case, after incubation with β -gal in PBS buffer, the longitudinal relaxivity of Gal-Cy-Gd-1 was

significantly enhanced with the activation of the NIR fluorescent signal (Figure S10 and Table 1), which was increased from 8.3 ± 0.3 to 14.2 ± 0.3 $\text{mM}^{-1} \text{s}^{-1}$ upon β -gal activation (20 MHz). In order to ensure an adequate nucleophilic environment that enables sufficient reaction of the resulting QMs intermediates, BSA was added, and the longitudinal relaxivity was further increased to 15.6 ± 0.3 $\text{mM}^{-1} \text{s}^{-1}$, which is about 2.9-fold higher than that of Dotarem (an MRI contrast agent in clinical practice, 5.4 ± 0.3 $\text{mM}^{-1} \text{s}^{-1}$). The elevated longitudinal relaxivity of Gal-Cy-Gd-1 after β -gal response can be attributed to the formation of a small molecule-protein labeling strategy with increased molecular weight, which lengthens the rotational correlation time τ_R of the small molecule and

shortens the T_1 of the water proton, resulting in brighter T_1 -weighted MR images (Figure 1i).

After demonstrating its ability of covalent labeling of protein, subsequently, we proceeded to move cellular imaging to visualize the β -gal activation of Gal-Cy-Gd-1 using NIR fluorescence and MRI. Before conducting the imaging experiments, the cytotoxicity of Gal-Cy-Gd-1 and Gal-Cy-Gd-2 were assessed using a standard MTT assay (Figure S11). The results demonstrated that both Gal-Cy-Gd-1 and Gal-Cy-Gd-2 had little effect on cell viability against human ovarian cancer cells (SKOV3) and normal human embryonic kidney cells (293T) at concentrations up to 100 μM , suggesting both Gal-Cy-Gd-1 and Gal-Cy-Gd-2 as biocompatible probes for cellular study.

Hence, we utilized Gal-Cy-Gd-1 to detect β -gal activity in living SKOV3 cells which has been demonstrated by overexpressing β -gal. Upon incubation with Gal-Cy-Gd-1 or Gal-Cy-Gd-2, the NIR-fluorescence intensity gradually increased inside the cells, peaking at 6 hours (Figure 3a, S12). Flow cytometry analysis at different time points supported these imaging results (Figure 3c, S13). To demonstrate the ability of self-immobilized probes based on the QMs structure to anchor to surrounding proteins following intracellular β -gal response, we co-incubated this pair of probes with SKOV3 cells for 6 hours. After removing any unbound fluorophores, we observed signifi-

Table 1: The longitudinal relaxivity (r_1) of the probes under different conditions.

MR probe	r_1 ($\text{mM}^{-1} \text{s}^{-1}$)	MR probe	r_1 ($\text{mM}^{-1} \text{s}^{-1}$)
Gal-Cy-Gd-1	8.3 ± 0.3	Gal-Cy-Gd-2	9.4 ± 0.3
Gal-Cy-Gd-1 + β -gal	14.2 ± 0.3	Gal-Cy-Gd-2 + β -gal	9.5 ± 0.3
Gal-Cy-Gd-1 + β -gal + BSA	15.6 ± 0.3	Gal-Cy-Gd-2 + β -gal + BSA	9.8 ± 0.3

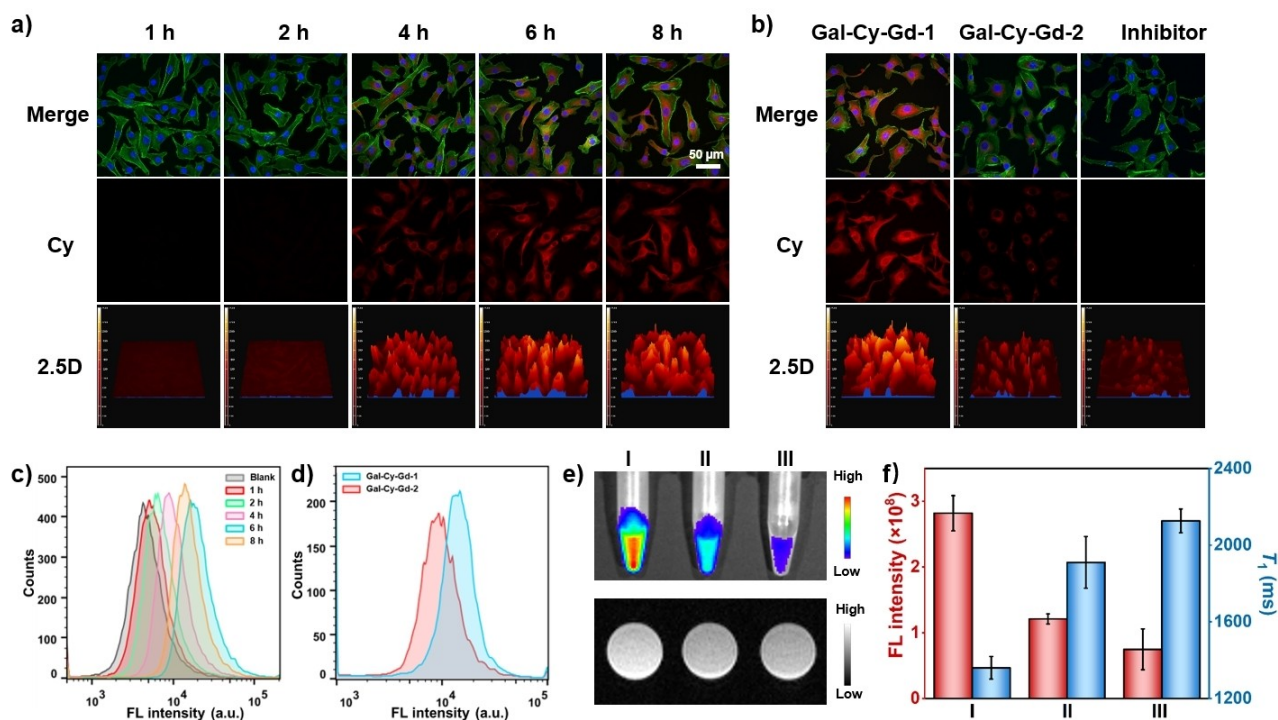


Figure 3. Imaging of β -gal activity in tumor cells. (a) NIR fluorescence images of SKOV3 cells at different time points after incubation with Gal-Cy-Gd-1. (b) NIR fluorescence images of SKOV3 cells with Gal-Cy-Gd-1 or Gal-Cy-Gd-2 (10 μM) were incubated at 37 $^{\circ}\text{C}$ for 6 h, as well as cells pretreated with D-(+)-ribonucleic acid-lactone, a β -gal inhibitor, for 30 min before incubation with Gal-Cy-Gd-1. (c) Flow cytometry of SKOV3 cells incubated with Gal-Cy-Gd-1 (10 μM) at 37 $^{\circ}\text{C}$ for 1–8 h. (d) Flow cytometry of SKOV3 cells incubated with Gal-Cy-Gd-1 or Gal-Cy-Gd-2 (10 μM). (e) Fluorescence (up) and T_1 -weighted MR (down) ($\text{TE/TR} = 5/500$ ms, 9.4 T) images of indicated cell pellets. $\lambda_{\text{ex/em}} = 710/760$ nm (I: Gal-Cy-Gd-1, II: Gal-Cy-Gd-2, III: Gal-Cy-Gd-1 + D-(+)-ribonucleic acid-lactone). (f) Comparison of the average FL intensity (red) and T_1 value (20 MHz, blue) of cell pellets in (e). ($n = 3$).

cantly stronger NIR fluorescence from the Gal-Cy-Gd-1-treated SKOV3 cells (Figure 3b, S12). Furthermore, incubation of Gal-Cy-Gd-1 with SKOV3 cells pretreated with the β -gal inhibitor D-(+)-ribonucleic acid-lactone resulted in minimal NIR fluorescence. To further compare the fluorescence of SKOV3 cells, we employed flow cytometry (Figure 3d), and the results were consistent with the earlier cell images. Specifically, the self-immobilized probe Gal-Cy-Gd-1, based on the QMs structure, exhibited a stronger fluorescence signal in SKOV3 cells compared to Gal-Cy-Gd-2, despite both probes showing similar fluorescence responses in aqueous solutions. Encouraged by the above results, we investigated NIR fluorescence and MR dual-modality imaging of β -gal activity in SKOV3 cell pellets. Figure 3e shows that the NIR fluorescence signals of SKOV3 cells incubated with Gal-Cy-Gd-1 (100 μ M, 6 h) were significantly stronger than those of other controls, which is consistent with the results of confocal fluorescence imaging of the cells (Figure 3b). Gal-Cy-Gd-1-treated SKOV3 cell pellets produced significant MR contrast enhancement, but inhibitor-treated SKOV3 cells and Gal-Cy-Gd-2-incubated SKOV3 cells had relatively lower MR signals. This difference may be due to the enhanced longitudinal relaxivity in

SKOV3 cells, which shortens the T_1 relaxation time of water protons in these cells (Figure 3f). These findings suggest that the self-immobilized probe based on the QMs structure restricts the diffusion of the activated fluorophore, leading to improved SBR and detection sensitivity.

To assess the suitability of Gal-Cy-Gd-1 for in vivo imaging, we studied the β -gal triggered activation of FL and MRI in live mice using a subcutaneous tumor model. The in vivo fluorescence imaging results revealed that mice intravenously injected with Gal-Cy-Gd-2 exhibited strong tumor fluorescence at 1 hour, but the fluorescence declined rapidly after 2 hours. In contrast, mice injected with Gal-Cy-Gd-1 (100 μ M, 100 μ L) showed a gradual enhancement in tumor fluorescence, reaching its peak at 24 hours, and was 1.5-fold higher than that of Gal-Cy-Gd-2-treated mice (Figure 4a, b). T_1 -weighted MR contrast of SKOV3 tumors also progressively increased upon intravenous (i. v.) injection of Gal-Cy-Gd-1 (0.02 mmol kg⁻¹ Gd³⁺), with the maximum signal enhancement in the tumor observed around 63 % at 4 hours (Figure 4e, f). H&E staining results confirmed that the probe has good biosafety and can be used for in vivo imaging (Figure S14). HPLC analysis of tumors dissected from mice 4 hours after Gal-Cy-Gd-1 injection showed that Gal-Cy-Gd-1 reacted in tumors and anchored to proteins

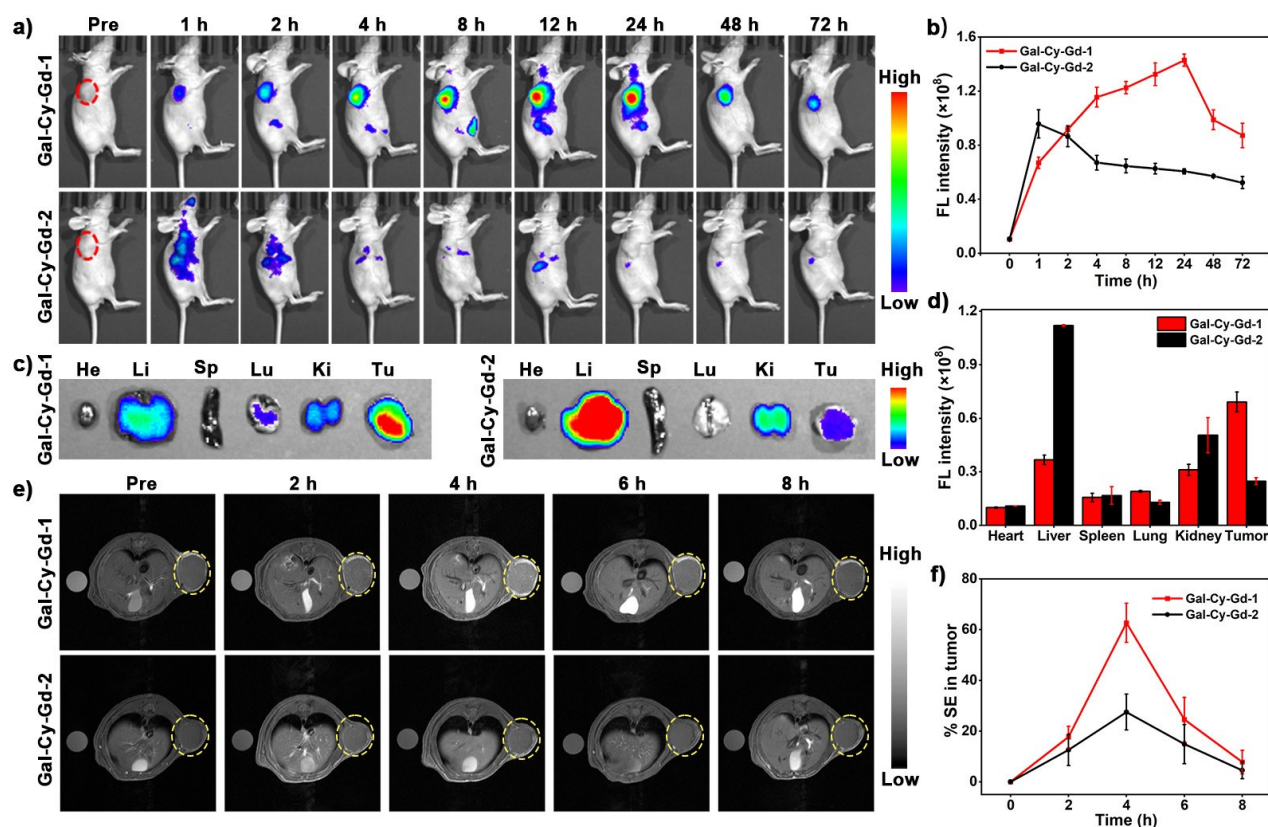


Figure 4. Bimodality imaging of endogenous β -gal in living mice of SKOV3 tumor. (a) FL imaging and (b) corresponding intensity of mice receiving i. v. injection of Gal-Cy-Gd-1 or Gal-Cy-Gd-2 (100 μ M, 100 μ L) at 0, 1, 2, 4, 8, 12, 24, 48 and 72 h. (c) Fluorescence images of tumor and main organs at 72 h after i. v. injection of Gal-Cy-Gd-1 or Gal-Cy-Gd-2. (d) Fluorescence intensity of organs and tumors in (c). $\lambda_{\text{ex/em}} = 710/760$ nm. (e) T_1 -weighted MR images and (f) % SE of SKOV3 tumor-bearing mice receiving i. v. injection of Gal-Cy-Gd-1 or Gal-Cy-Gd-2 (0.02 mmol kg⁻¹ Gd³⁺). Images were acquired before (Pre), 2, 4, 6 and 8 h after i. v. injection at 9.4 T MRI, with TE/TR = 6/600 ms.

(Figure S15). These results demonstrate that Gal-Cy-Gd-1 has the ability to diffuse into tumor tissues, become activated, and label the target, making it a promising probe for *in vivo* imaging.

After 72 hours post-injection, we excised major organs and tumors for *ex vivo* fluorescence imaging to investigate the biodistribution of Gal-Cy-Gd-1 and Gal-Cy-Gd-2 (Figure 4c, d). Notably, Gal-Cy-Gd-1-treated tumors exhibited the brightest fluorescence among all excised tissues, with an intensity approximately 1.9 times that of the liver. The liver displayed the highest fluorescence intensity among all excised tissues and tumors treated with Gal-Cy-Gd-2, and it was much higher than tumor tissues. Moreover, the fluorescence intensity of Gal-Cy-Gd-1-treated tumors was approximately 2.8-fold higher than that of Gal-Cy-Gd-2-treated tumors. ICP-MS analysis demonstrated that the ID % g^{-1} of Gal-Cy-Gd-1-treated tumors ($\approx 17.1\%$) was approximately 4.2-fold higher than that of Gal-Cy-Gd-2-treated tumors ($\approx 4.0\%$) (Figure S16). These results confirmed the enhanced fluorescence and MR contrast observed non-invasively in living mice, indicating that β -gal-mediated fluorescence reaction and enzymatic self-immobilizing effectively activated Gal-Cy-Gd-1, leading to increased β -gal-associated accumulation in tumors.

Taking advantage of the β -gal-mediated fluorescence reaction and enzyme self-immobilizing for targeted local-

ization in tumor tissues, we utilized Gal-Cy-Gd-1 to visualize and guide the resection of *in situ* SKOV3 ovarian tumors. To establish mouse ovarian tumors *in situ*, we injected luciferase-transfected SKOV3 cells (SKOV3/Luc) into the left ovary of mice. After four weeks, strong bioluminescence (BL) and H&E staining both confirmed successful tumor growth (Figure S17). Upon *i.v.* injection of Gal-Cy-Gd-1, we observed bright NIR fluorescence specifically in the left ovary of SKOV3/Luc tumor mice, precisely matching the BL imaging region. In contrast, the fluorescence and BL signals were barely visible in normal ovary mice (Figure 5a). Additionally, we noticed higher T_1 -weighted MR contrast in the ovarian tumor region following the injection of Gal-Cy-Gd-1 (Figure 5b). These results convincingly demonstrate the effective accumulation of Gal-Cy-Gd-1 in the location of *in situ* ovarian tumors in living mice through NIR fluorescence and MR imaging. Building upon these findings, we conducted image-guided surgical resection of *in situ* SKOV3/Luc tumors in intraoperative mice by administering Gal-Cy-Gd-1 through the tail vein. Ten hours post-injection, the tumor site exhibited stronger fluorescence compared to the surrounding tissues, accurately delineating the margins of the ovarian tumor and enabling precise surgical resection of the tumor tissue (Figure 5c). Intraoperative BL imaging further confirmed the successful excision of

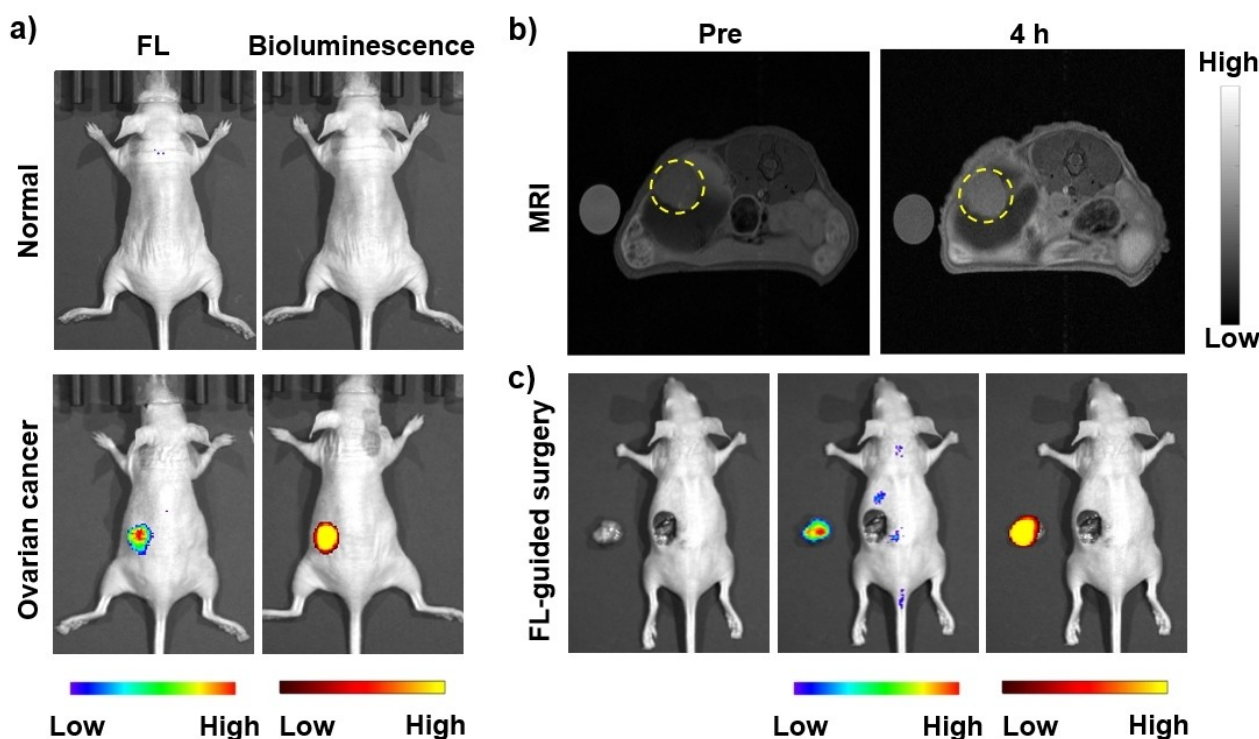


Figure 5. Bimodality imaging and fluorescence-guided surgery of orthotopic ovarian tumors. (a) Whole-body fluorescence (left) and bioluminescence (right) imaging of normal mice and orthotopic SKOV3/Luc ovarian tumor xenograft mice. The fluorescence images were acquired in living mice following *i.v.* injection of Gal-Cy-Gd-1 (100 μM , 100 μL) at 10 h ($\lambda_{\text{ex/em}} = 710/760$ nm). (b) T_1 -weighted MR imaging of orthotopic SKOV3/Luc ovarian tumor xenograft mice. Images were acquired before and 4 h post *i.v.* injection of Gal-Cy-Gd-1 (0.02 mmol kg^{-1}) at 9.4 T. Yellow dotted circles indicate the location of the tumor in the ovary. (c) Imaging-guided surgical resection of orthotopic SKOV3/Luc ovarian tumor after *i.v.* injection of Gal-Cy-Gd-1 (100 μM , 100 μL) at 10 h.

the tumor from the ovary, establishing Gal-Cy-Gd-1 as a promising molecular imaging tool for guiding in situ ovarian tumor surgery.

Conclusion

In conclusion, this study presents a new activatable bimodal probe called Gal-Cy-Gd-1, which is based on the QMs structure. It enables real-time β -gal activity imaging in vivo using NIR fluorescence and MRI. Through various in vitro and in vivo experiments, we have confirmed that Gal-Cy-Gd-1 exhibits a significant increase in fluorescence intensity upon β -gal activation. It also selectively labels nearby target enzymes or proteins, preventing rapid probe diffusion from the site of interest and enhancing the MRI signal. The simultaneous enhancement of NIR fluorescence and longitudinal relaxivity allows for the non-invasive measurement and localization of β -gal activity in live tumor cells and mice. Moreover, we effectively utilized Gal-Cy-Gd-1 to guide the intraoperative resection of ovarian tumors in mice, enabling real-time visualization during the surgery. This study showcases the strong in vivo imaging potential of Gal-Cy-Gd-1 in detecting β -gal activity in tumors. Looking forward, this approach has the potential to facilitate the development of activatable probes that synergistically combine NIR fluorescence with other imaging techniques, such as photoacoustic imaging, positron emission tomography (PET), and computed tomography (CT). This advancement holds promising implications for precise drug delivery control in cancer therapy.

Supporting Information

Experimental details include synthesis and characterization, enzyme reactivity and selectivity of the probes, competition studies, cellular and calculation.

Acknowledgements

This work was supported by the National Key R&D Program of China (2018YFA0704000), the National Natural Science Foundation of China (U21A20392, 82127802 and 21921004), the Hubei Provincial Natural Science Foundation of China (grant no. 05182321). Xin Zhou acknowledges the support from the Tencent Foundation through the XPLOER PRIZE, and Shizhen Chen acknowledges the support from the Young Top-notch Talent Cultivation Program of Hubei Province.

Conflict of Interest

The authors declare no conflict of interest.

Data Availability Statement

The data that support the findings of this study are available in the supplementary material of this article.

Keywords: Bimodal Imaging · Image-Guided Surgery · MRI · β -Gal Activity

- [1] a) S. I. Kim, N. Kang, S. Leem, J. Yang, H. Jo, M. Lee, H. S. Kim, D. N. Dhanasekaran, Y. K. Kim, T. Park, Y. S. Song, *Cancers* **2020**, *12*, 1309; b) E. Minis, K. Holcomb, G. Sisti, D. Nasioudis, T. T. Kanninen, A. Athanasiou, M. K. Frey, E. Chapman-Davis, T. A. Caputo, S. S. Witkin, *Eur. J. Obstet. Gynecol. Reprod. Biol.: X* **2019**, *2*, 100012.
- [2] a) S. Narod, *Nat. Rev. Clin. Oncol.* **2016**, *13*, 255–261; b) H. I. Jang, S. H. Lim, Y. Y. Lee, T. J. Kim, C. H. Choi, J. W. Lee, B. G. Kim, D. S. Bae, *Obstet. Gynecol. Sci.* **2017**, *60*, 170–177.
- [3] a) Y. Yang, B. Wang, X. Zhang, H. Li, S. Yue, Y. Zhang, Y. Yang, M. Liu, C. Ye, P. Huang, X. Zhou, *Adv. Mater.* **2023**, *35*, 2211337; b) S. Chen, L. Xiao, Y. Li, M. Qiu, Y. Yuan, R. Zhou, C. Li, L. Zhang, Z. X. Jiang, M. Liu, X. Zhou, *Angew. Chem. Int. Ed.* **2022**, *61*, e202213495; c) R. Yan, Y. Hu, F. Liu, S. Wei, D. Fang, A. J. Shuhendler, H. Liu, H. Y. Chen, D. Ye, *J. Am. Chem. Soc.* **2019**, *141*, 10331–10341.
- [4] a) N. S. Galenkamp, M. Soskine, J. Hermans, C. Wloka, G. Maglia, *Nat. Commun.* **2018**, *9*, 4085; b) J. Zhao, C. Wang, W. Sun, C. Li, *Adv. Mater.* **2022**, *34*, 2203667; c) D. J. Waterhouse, C. R. M. Fitzpatrick, B. W. Pogue, J. P. B. O'Connor, S. E. Bohndiek, *Nat. Biomed. Eng.* **2019**, *3*, 339–353.
- [5] a) H. Liu, L. Chen, C. Xu, Z. Li, H. Zhang, X. Zhang, W. Tan, *Chem. Soc. Rev.* **2018**, *47*, 7140–7180; b) J. Zhang, X. Chai, X.-P. He, H.-J. Kim, J. Yoon, H. Tian, *Chem. Soc. Rev.* **2019**, *48*, 683–722.
- [6] a) S. K. Lee, Z. Shen, M. S. Han, C. H. Tung, *RSC Adv.* **2022**, *12*, 4543–4549; b) H. Pan, X. Chai, J. Zhang, *Chin. Chem. Lett.* **2023**, *34*, 108321.
- [7] a) R. Liu, H. Chen, S. Zhang, B. Zhao, L. Zhou, F. Zhang, X. Nie, J. Liu, *Sens. Actuators B* **2022**, *372*, 132660; b) K. Gu, W. Qiu, Z. Guo, C. Yan, S. Zhu, D. Yao, P. Shi, H. Tian, W.-H. Zhu, *Chem. Sci.* **2019**, *10*, 398–405.
- [8] a) Z. He, Z. Qiu, L. Liao, C. Zhang, S. Hu, S. Zhao, *Sens. Actuators B* **2023**, *381*, 133423; b) Y. Zhou, P. Lei, J. Han, Z. Wang, A. Ji, Y. Wu, L. Zheng, X. Zhang, C. Qu, J. Min, W. Zhu, Z. Xu, X. Liu, H. Chen, Z. Cheng, *J. Med. Chem.* **2023**, *66*, 1210–1220; c) S. Roy, N. Bag, S. Bardhan, I. Hasan, B. Guo, *Adv. Drug Delivery Rev.* **2023**, *197*, 114821.
- [9] a) Y. Wang, Y. Hu, D. Ye, *Angew. Chem. Int. Ed.* **2022**, *61*, e202209512; b) Q. Li, X. Xue, J. Wang, Y. Ye, J. Li, Y. Ren, D. Wang, B. Liu, Y. Li, L. Zhao, Q. Xu, *Anal. Chem.* **2022**, *94*, 11255–11263; c) L. Wang, Q. Wan, R. Zhang, B. Situ, K. Ni, J. Gao, X. Feng, P. Zhang, Z. Wang, A. Qin, B. Tang, *ACS Nano* **2021**, *15*, 9924–9934.
- [10] a) J. Li, K. Pu, *Chem. Soc. Rev.* **2019**, *48*, 38–71; b) Z. Qin, T.-B. Ren, H. Zhou, X. Zhang, L. He, Z. Li, X.-B. Zhang, L. Yuan, *Angew. Chem. Int. Ed.* **2022**, *61*, e202201541.
- [11] a) J. Wahsner, E. M. Gale, A. Rodriguez-Rodriguez, P. Caravan, *Chem. Rev.* **2019**, *119*, 957–1057; b) J. H. Tang, H. Li, C. Yuan, G. Parigi, C. Luchinat, T. J. Meade, *J. Am. Chem. Soc.* **2023**, *145*, 10045–10050.
- [12] a) V. S. Harrison, C. E. Carney, K. W. MacRenaris, E. A. Waters, T. J. Meade, *J. Am. Chem. Soc.* **2015**, *137*, 9108–9116; b) C. Li, L. Cao, Y. Zhang, P. Yi, M. Wang, B. Tan, Z. Deng, D. Wu, Q. Wang, *Small* **2015**, *11*, 4517–4525.
- [13] J. Huang, K. Pu, *Angew. Chem. Int. Ed.* **2020**, *59*, 11717–11731.

- [14] a) Y. Zhang, W. Li, X. Chen, S. Xiong, Y. Bian, L. Yuan, X. Gao, D. Su, *Anal. Chem.* **2023**, *95*, 2579–2587; b) X. Zhang, S. Shen, D. Liu, X. Li, W. Shi, H. Ma, *Chem. Sci.* **2023**, *14*, 2928–2934.
- [15] a) Y. Wang, X. Hu, J. Weng, J. Li, Q. Fan, Y. Zhang, D. Ye, *Angew. Chem. Int. Ed.* **2019**, *58*, 4886–4890; b) C. Wu, R. Zhang, W. Du, L. Cheng, G. Liang, *Nano Lett.* **2018**, *18*, 7749–7754.
- [16] a) X. Wu, R. Wang, N. Kwon, H. Ma, J. Yoon, *Chem. Soc. Rev.* **2022**, *51*, 450–463; b) S. Uchinomiya, T. Nagaura, M. Weber, Y. Matsuo, N. Zenmyo, Y. Yoshida, A. Tsuruta, S. Koyanagi, S. Ohdo, N. Matsunaga, A. Ojida, *J. Am. Chem. Soc.* **2023**, *145*, 8248–8260.

Manuscript received: September 5, 2023

Accepted manuscript online: September 27, 2023

Version of record online: October 13, 2023